

The Effects of Preionization Level on a 'Stabilized' Z-pinch

C. Silawatshanantai,^{A,B} F. S. B. Anderson,^A M. H. Brennan,^A
G. Durance,^{A,C} I. R. Jones,^A E. L. Murray^A and J. Tendys^{A,C}

^A School of Physical Sciences, Flinders University of South Australia,
Bedford Park, S.A. 5042.

^B Present address: Department of Physics, Prince of Songkla University,
Haad-Yai, Thailand.

^C Visiting Scholar, on attachment from the Australian Atomic Energy Commission.

Abstract

The influence of the degree of preionization on the formation and properties of a conventional 'stabilized' Z-pinch has been studied experimentally for preionization levels ranging from 2% to 35%. It is concluded that there exists the possibility of using varying levels of preionization to tailor radial profiles of density and pressure, and hence to influence the value of β_0 .

1. Introduction

The plasma physics group at Flinders University has embarked upon a reinvestigation of the 'stabilized' linear Z-pinch with the aim of providing detailed experimental information relevant to the reversed field pinch configuration. Preliminary investigations were carried out in a prototype device (Weber *et al.* 1976) known as FUZA-1 (Flinders University Z-pinch Apparatus-1). The studies are now being continued in FUZA-2, which is longer, designed to handle larger plasma currents, and equipped with a superior vacuum and gas-handling system.

The experiments reported here concern the influence of the level of preionization on the dynamics and properties of the pinch. Although there is much folklore concerning the effects of preionization in pinch physics, the information to be found in the open literature is sparse. Nevertheless, the degree of preionization has been observed to affect:

- (1) the rate of magnetic field penetration during the implosion phase of SCYLLA-1B (Gribble *et al.* 1974);
- (2) the effectiveness of shock compression in a hard-core pinch (Koppendorfer 1963);
- (3) the fast compressional heating in the Garching belt pinch, ISAR-IV (Krause *et al.* 1973);
- (4) the rate of rise and degree of bouncing of the on-axis electron temperature in HBTX (Gowers *et al.* 1972; Newton *et al.* 1972);
- (5) the diamagnetism in a theta-pinch (Green *et al.* 1966);
- (6) the stability in SPICA (Bobeldijk *et al.* 1978) and ZT-1 (Baker *et al.* 1973);
- (7) the radial pressure profile in ZT-1 (Burkhardt *et al.* 1972).

Although the above results largely confirm what one may intuitively expect, namely that a higher level of preionization reduces the rate of magnetic field pene-

tration leading to more effective shock heating, more quantitative information over a wide range of experimental conditions is nevertheless desirable.

To summarize the results of the present study, it is convenient to divide the plasma discharge into three distinct phases: the formative phase which includes the initial implosion and bounce, the equilibrium phase where the plasma motion is negligible and pressure balance is obtained, and the unstable phase corresponding to the onset of gross instabilities. During the formative phase, low levels of preionization were found to lead to rapid magnetic field penetration with very little 'bouncing'. However, the time to reach peak compression (i.e. maximum B_z on-axis and minimum plasma radius) and the line density of the compressed plasma were found to be almost independent of preionization level. On the other hand, in the equilibrium phase, the radial pressure and temperature profiles and the value of β_θ (i.e. the ratio of the average plasma pressure to the azimuthal field pressure at the plasma boundary) were found to be dependent on preionization level. The unstable phase was not studied in detail.

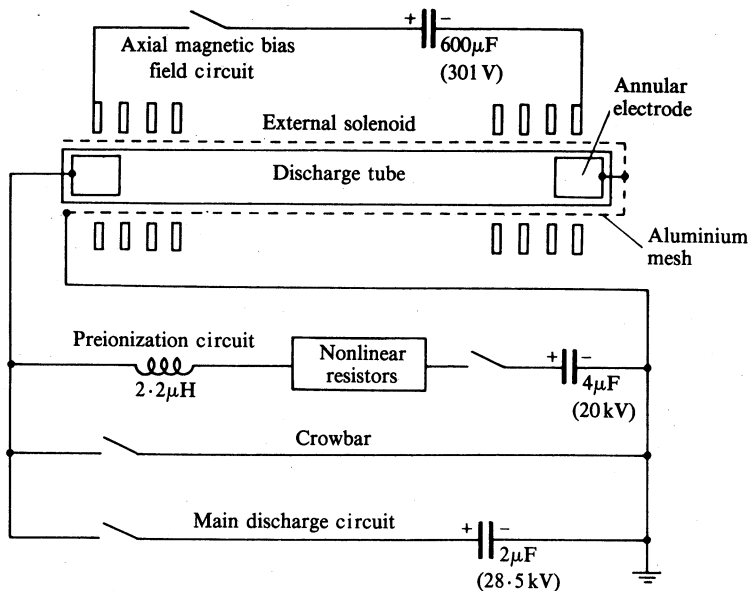


Fig. 1. Schematic circuit diagram of FUZA-2.

2. Description of FUZA-2

The cylindrical discharge vessel consisted of a Pyrex tube of inside diameter 10.4 cm with annular stainless steel electrodes of 9.5 cm inner diameter located at each end. The interelectrode spacing was 1.65 m. The discharge tube was surrounded by an aluminium mesh of inner diameter 12.6 cm which acted as the return conductor for the plasma current and also as a flux-conserving wall. An axial bias field was produced by an external solenoid of 20 identical pancake coils. The coil spacing was constant except for the outermost coils which were positioned to provide a uniform field over the region between the two electrodes. A tailored single half sine-wave current pulse was used to preionize the filling gas and a conventional crowbarred capacitor discharge provided the main discharge current. A schematic circuit diagram of the apparatus is shown in Fig. 1.

A fast piezo-electric valve was used to admit a fixed charge of gas into the discharge tube prior to each shot. Between shots the tube was pumped back down to base pressure (10^{-7} torr). Before each experimental run, the discharge tube was cleaned by passing the preionization current for about 20 shots followed by a similar number of main discharge current shots. However, the effect of discharge cleaning on the properties of the pinched plasma was not investigated.

The experimental conditions are shown in Table 1. The choice of gas filling pressure and bias field was based largely on the results from the earlier FUZA-1 experiments.

Table 1. Experimental conditions in FUZA-2

Filling gas	Deuterium ^A
Filling gas pressure	35 mtorr (4.67 Pa)
Axial magnetic field	235 G ^B (23.5 mT)
Preionization current pulse	Half sine-wave 13.0 kA peak 11.6 μ s duration
Main discharge current	35–37 kA peak $5\text{--}7 \times 10^{10}$ A s ⁻¹ rate of current rise ~ 20 μ s decay constant

^A Purified by filtering through a palladium thimble.

^B Lines of initial B_z point from anode to cathode.

3. Level of Preionization

Fig. 2 shows a typical oscillogram of the preionization and main pinch currents. The level of preionization was varied by delaying the commencement of the main discharge current (by a time t_d) from the end of the preionization current pulse. The level of preionization at the various delay times t_d was determined using the laser interferometry technique pioneered by Ashby and Jephcott (1963). The radial profile of the electron density $n_e(r)$ in the preionized plasma is shown in Fig. 3 for different t_d . Measurements beyond $r = 4$ cm were precluded by the presence of the annular electrodes at each end of the discharge tube.

The level of preionization is defined as the ratio of electron line density $N_e(t)$ to the initial atom line density N_0 corresponding to the filling pressure, where

$$N_e(t) = 2\pi \int_0^{r_g} n_e(r) dr,$$

and r_g is the inner wall radius of the glass vacuum vessel. The values of $n_e(r)$ were obtained from Fig. 3 using the 'smooth' extrapolations (long-dashed curve) for $r > 4$ cm. Because of the r^2 weighting this section made a very large contribution to the above integral. (Approximately 40% of the cross-sectional area of the tube was contained in this outer region.) The resulting levels of preionization were as follows, where the upper error limits correspond to the line densities obtained using the 'tangential' extrapolations (Fig. 3) and the lower limits were obtained by assuming that the density falls linearly to zero between $r = 4$ cm and $r = 5.2$ cm ($=r_g$):

Time delay t_d (μ s)	1	30	50	100
$N_e(t)/N_0$ (%)	35 ± 7	16 ± 2	8 ± 1	2.1 ± 0.1

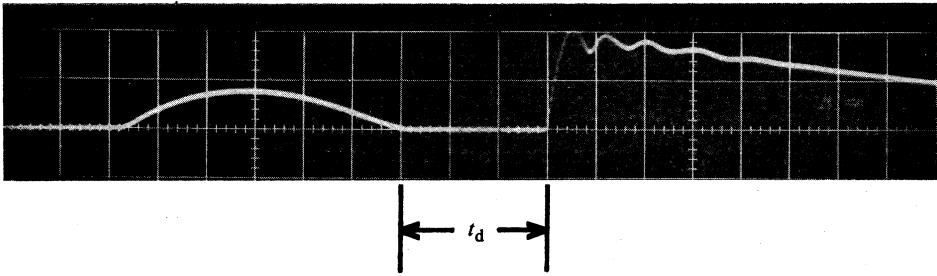


Fig. 2. Preionization and main discharge current waveforms. (Vertical scale is 18 kA per grid line; horizontal scale $2 \mu\text{s}$ per grid line.)

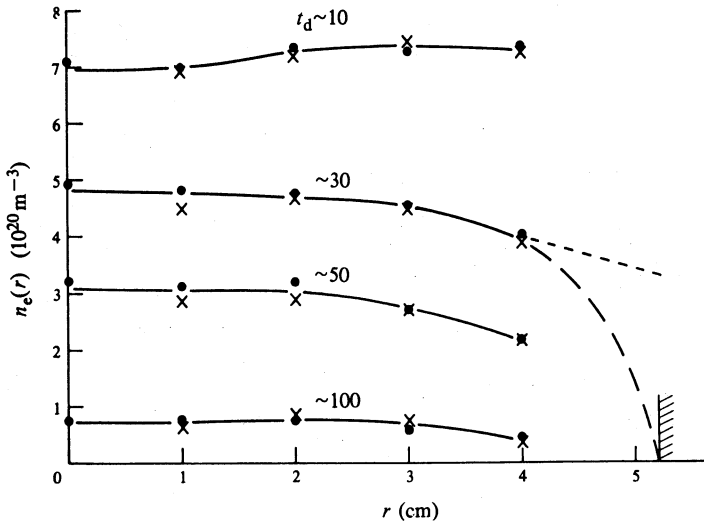


Fig. 3. Radial profile of the preionized plasma density $n_e(r)$ for different t_d (in μs). Dots and crosses denote radial positions to the right and left of the discharge tube axis (as seen from the cathode). Solid curves are to guide the eye, while the short-dashed and long-dashed curves are tangential and 'smooth curve' extrapolations.

It is seen that the chosen values of initial gas filling pressure, bias field and preionization circuitry result in levels of preionization ranging from 35% (at $t_d = 1 \mu\text{s}$) to 2% (at $t_d = 100 \mu\text{s}$). Moreover the preionized plasma is seen to be uniformly distributed across most of the diameter for all levels of preionization.

4. Experimental Results

(a) Streak Photography

To gain qualitative insight into the effects of the degree of preionization upon the main discharge, end-on streak photographs were taken using an Imacon HE-700 image converter camera. These are shown in Fig. 4. They clearly show that the plasma implodes in a time $\sim 1.8 \mu\text{s}$ which is followed by a period of strong plasma bounce for a further $\sim 1.5 \mu\text{s}$. Following this the plasma appears to relax to an equilibrium configuration.

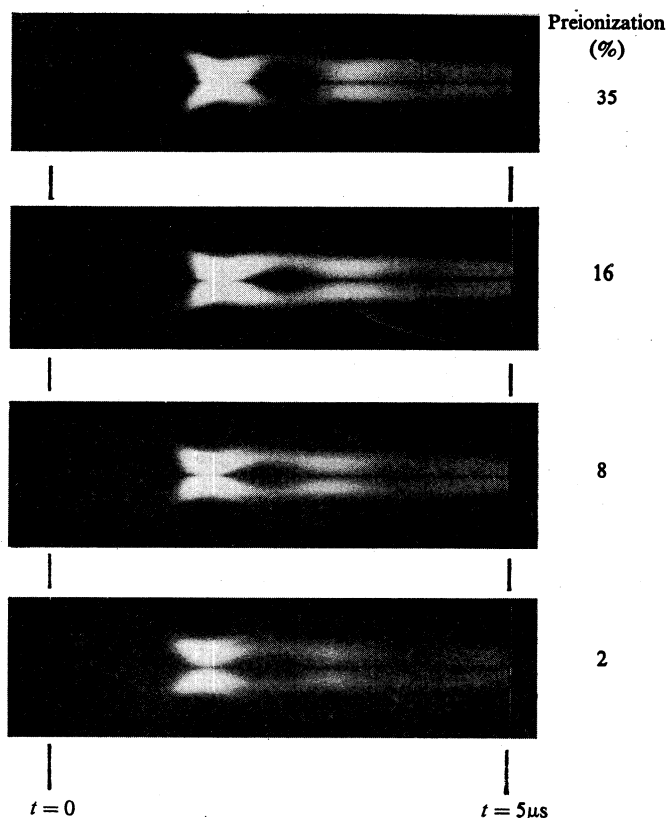


Fig. 4. Streak photographs of a pinch discharge for different preionization levels.

It can be seen from these photographs that the time to reach maximum compression appears to be independent of the preionization level, whereas the actual degree of bounce appears more marked at higher preionization levels. The lack of luminosity at the walls indicates that no wall breakdown occurred for any of the experimental conditions.

Also in evidence in the photograph for the 2% preionization case is the division of the plasma column into two coaxial layers with the outer layer expanding towards the wall of the discharge vessel. This has been positively identified as being associated with the formation of a reversed current in the outer sheath which then expands under the influence of an outwardly directed $\mathbf{j} \times \mathbf{B}$ force. Observation of the reversed current and ejection of the outer sheath have been discussed in detail by Jones and Silawatshananai (1980).

(b) Power

The power inputs into the system, derived from voltage and current measurements, are shown in Fig. 5 for the extreme cases of 35% and 2% preionization; the other cases are intermediate between these. Only minor differences are evident during the implosion ($t < 2 \mu\text{s}$). The effect of plasma bounce ($2 < t < 3 \mu\text{s}$) is seen to diminish at low levels of preionization, consistent with the streak photographs. After

this period there is little net electrical energy flow into or out of the discharge region—the equilibrium phase.

(c) *Magnetic Fields*

The spatial and temporal behaviour of the axial and azimuthal magnetic field components B_z and B_θ during the main discharge were measured for the four preionization levels. A miniature magnetic probe (20 turns in a volume of $3.0 \times 0.7 \times 0.7 \text{ mm}^3$) was used for these measurements. Field profiles at different times in the discharge are shown in Figs 6–8 as smooth curves through data points obtained from a large number of shots.

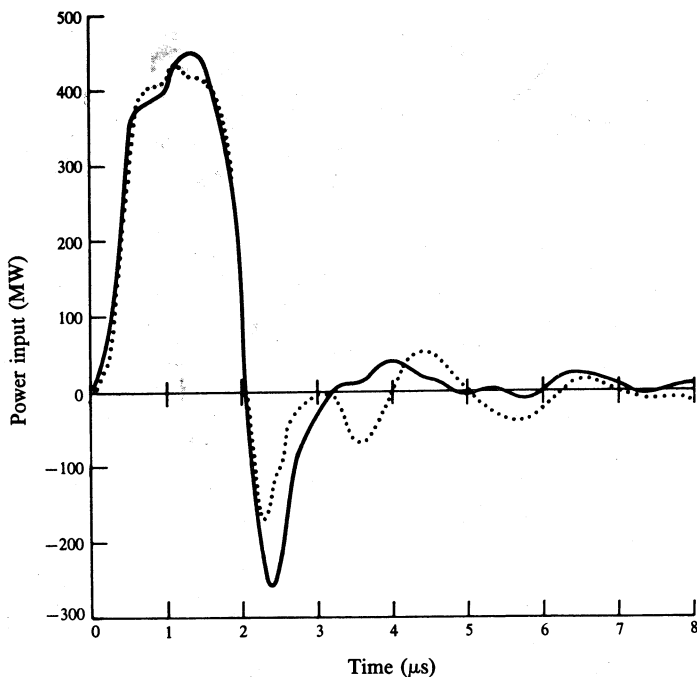


Fig. 5. Power input to the discharge vessel for 35% (solid curve) and 2% (dotted curve) preionization.

Figs 6 and 7 show the behaviour of the magnetic field components during the implosion for the 35% and 2% preionization levels. One notes the rapid penetration of the azimuthal field and the corresponding rapid rise of the axial field, at small radii, for the weakly preionized plasma. The profiles are seen to be symmetric for both levels of preionization.

Fig. 8 shows the behaviour of the field profiles at $t = 3.5 \mu\text{s}$, that is, in the equilibrium phase. The error bars shown on the B_z profiles of Fig. 8 are based upon the scatter in the data. A similar small scatter was also found in the B_θ profiles. Additionally, however, a slight asymmetry was found for all the B_θ profiles, the extent of which is shown by the error bars. No analogous asymmetry was apparent in any B_z profiles. It should be noted that the small scatter signifies a high degree of shot-to-shot reproducibility, since each profile is a composite of many separate shots.

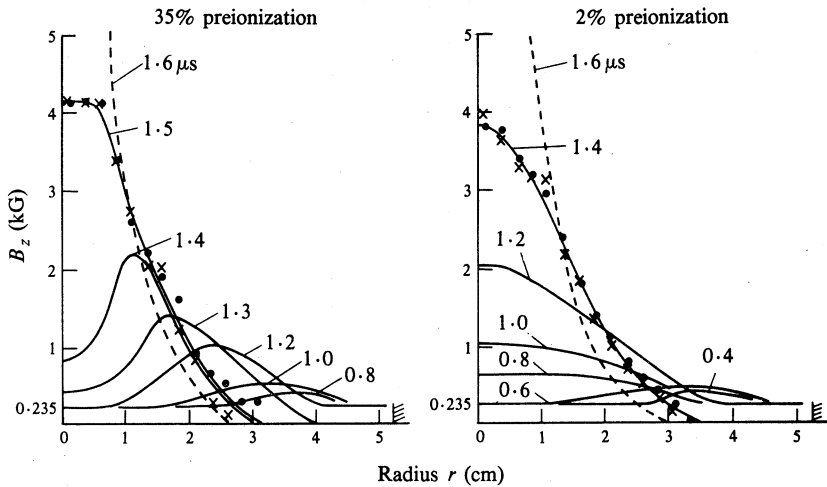


Fig. 6. Profiles of the axial magnetic field B_z during the implosion. Actual data points are shown for $t = 1.4$ and $1.5 \mu\text{s}$ (for 2% and 35% preionization respectively), with dots and crosses denoting radial positions to the right and left of the discharge tube axis (as seen from the cathode).

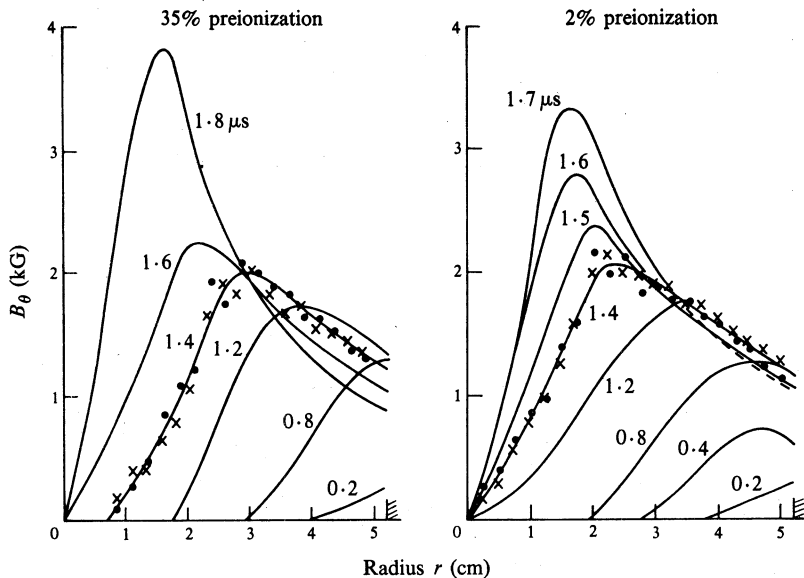


Fig. 7. Profiles of the azimuthal magnetic field B_θ during the implosion. Actual data points are shown for $t = 1.4 \mu\text{s}$ for both 2% and 35% preionization, with dots and crosses denoting radial position to the right and left of the discharge tube axis (as seen from the cathode).

Corresponding field profiles at $t = 6.5 \mu\text{s}$ exhibited large scatter which suggests that the plasma has developed an instability by this stage of the discharge.

In interpreting the results shown in Fig. 8, it should be noted that, because there were extended periods of time between measurements at different preionization levels and also difficulties in maintaining accurate calibration of the instrumentation, there is a small systematic uncertainty between the results for the different preionization levels.

The actual variation with preionization level of the peak magnetic fields at $t = 3.5 \mu\text{s}$ may therefore be less than that shown in Fig. 8. Indeed, a separate measurement of the on-axis B_z for a range of preionization levels showed the peak field at $t = 3.5 \mu\text{s}$ to be independent of preionization level. The results of this measurement are shown in Fig. 9. Also shown are the on-axis fields at the time of peak compression ($t \sim 1.8 \mu\text{s}$) and at the time of the first bounce when the plasma radius reaches a maximum ($t \sim 2.6 \mu\text{s}$).

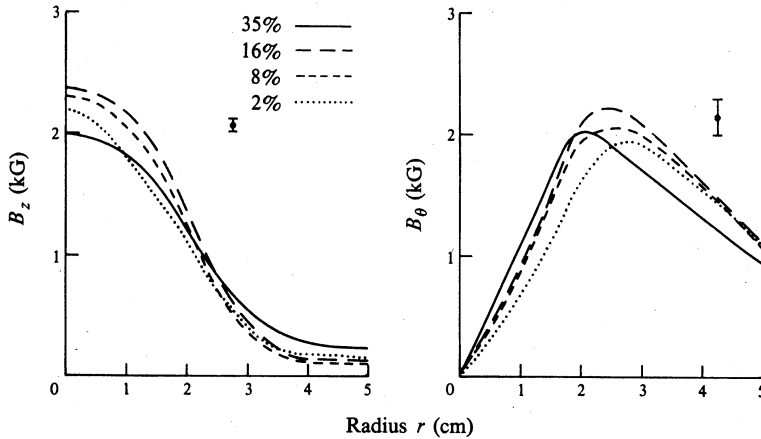


Fig. 8. Axial B_z and azimuthal B_θ magnetic field profiles at $t = 3.5 \mu\text{s}$ for 35%, 16%, 8% and 2% preionization. Typical error bars are shown for each field component.

(d) Currents

By using Maxwell's equations, the axial current density was derived from the above profiles, and the results for $t = 3.5 \mu\text{s}$ are shown in Fig. 10. It is seen that the current profiles are hollow for all levels of preionization, and that the profiles broaden as the preionization level is decreased. Essentially all of the current flows within a radius of ~ 4 cm; there is no evidence of current flow near the wall of the discharge vessel (which is consistent with the streak photographs in Fig. 4). This latter observation is confirmed by the results shown in Table 2 where the total currents obtained by integration of the profiles of Fig. 10 are compared with those measured by a Rogowski coil surrounding the discharge vessel.

(e) Holographic Interferometry

Double exposure holographic interferometry was used to determine electron densities at selected times in the discharge. The output from an amplified Korad K-1Q pulsed ruby laser (180 mJ output with a pulse width of 40 ns) was split into a 'scene' beam passing through the discharge region and a reference beam which were then recombined at a holographic plate (Agfa 10E75). The method is described in more detail by Jahoda and Sawyer (1971). Background fringes were incorporated for ease of interpretation and accuracy.

A set of interferograms showing the temporal evolution of the plasma for the 35% preionization condition is shown in Fig. 11. Similar sets of interferograms were

taken for each of the four preionization levels. The implosion is clearly seen with peak compression being reached at $t \sim 1.8 \mu\text{s}$. This time to peak compression was found to be independent of the initial preionization level. Electron density profiles during the implosion, obtained from the interferograms in Fig. 11, are shown in Fig. 12. They are generally similar to the axial magnetic field profiles of Fig. 6. Fig. 13a compares the density profiles at $t = 1.8 \mu\text{s}$ for the four levels of preionization.

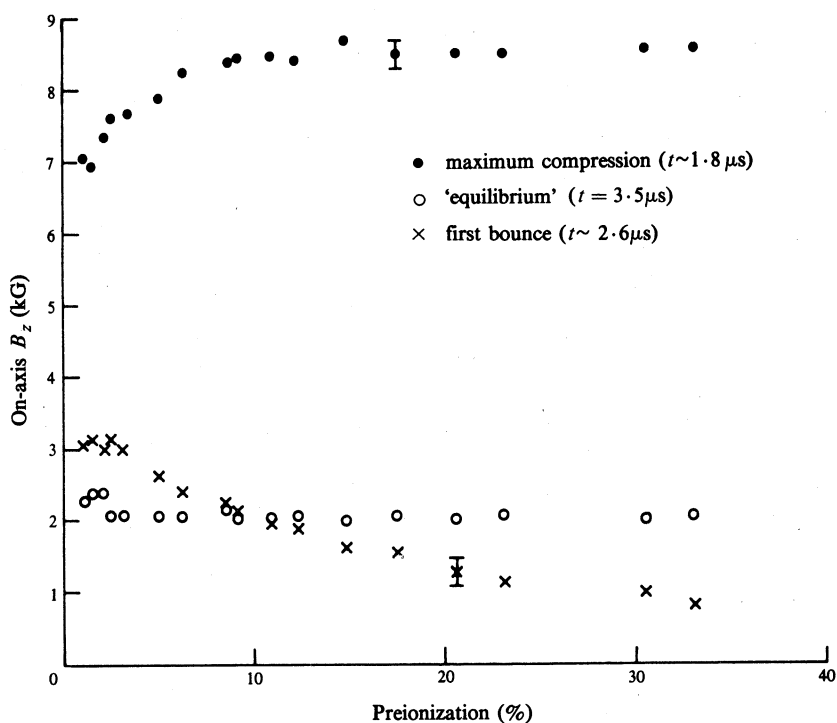


Fig. 9. On-axis axial magnetic field B_z as a function of preionization level for $t = \sim 1.8$, 3.5 and $\sim 2.6 \mu\text{s}$.

The profiles at this time, close to peak compression, are symmetric and quite hollow with a drop in the value of peak density with decreasing preionization level. Integrating these density profiles to obtain the ratio of the electron line density to the initial atom line density yields the following:

Preionization (%)	35	16	8	2
Ratio (%)	77	67	75	65

Thus, at the time of peak compression, this ratio is relatively insensitive to the initial level of preionization.

Density profiles at $t = 3.5 \mu\text{s}$ for each preionization level are shown in Fig. 13b. The profiles are symmetric and, despite the significant differences between the density profiles at the time of peak compression (Fig. 13a), they do not differ greatly: the level of preionization has a much smaller influence on the density profiles of the equilibrium plasma.

It should be noted that each profile was obtained from a single shot, and therefore provides no indication of shot-to-shot reproducibility (in contrast to the magnetic field profiles).

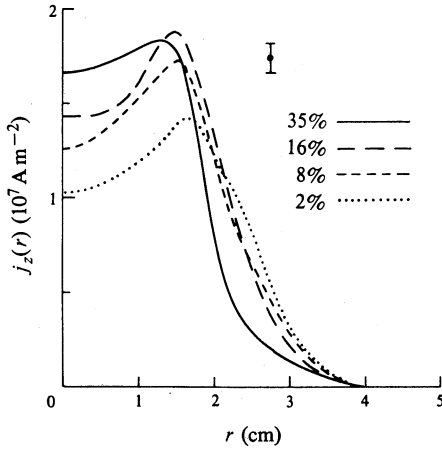


Fig. 10. Axial current density $j_z(r)$ at $t = 3.5 \mu\text{s}$ for 35%, 16%, 8% and 2% preionization.

Table 2. Total axial current at $t = 3.5 \mu\text{s}$

Preionization (%)	Integrated Rogowski coil signal (kA)	Integrated current density (kA)
35	28.4 ± 1.4	27 ± 3
16	31.4 ± 1.6	38 ± 4
8	29.5 ± 1.5	32 ± 4
2	30.8 ± 1.6	31 ± 4

(f) Plasma Temperature

In the absence of macroscopic plasma acceleration, the sum of the electron and ion temperatures $T_e + T_i$ may be obtained from the pressure balance relation

$$p(r) = n_e(r) k \{T_e(r) + T_i(r)\} \\ = \frac{1}{2\mu_0} \left(B_z^2(r_g) + B_\theta^2(r_g) - B_z^2(r) - B_\theta^2(r) \right) + \frac{1}{\mu_0} \int_r^{r_g} \frac{B_\theta^2(r')}{r'} dr',$$

where r_g is the inner radius of the discharge tube and $p(r_g)$ is assumed to be zero (i.e. the plasma is confined entirely by the fields).

In addition to the requirement that plasma acceleration effects must be small, the determination of temperature using the pressure balance relation requires accurately determined, and axially symmetric, electron density and magnetic field profiles. These combined criteria suggest that the technique can only be confidently applied at $t \sim 3.5 \mu\text{s}$. Application of the technique for this time yields the profiles of $T_e + T_i$ shown in Fig. 14.

The temperature profiles shown in Fig. 14 are displayed for $r \leq 2$ cm: at larger radii, the systematic errors in the determination of pressure (arising from the asymmetries in the B_θ profiles) preclude meaningful determinations of temperature.

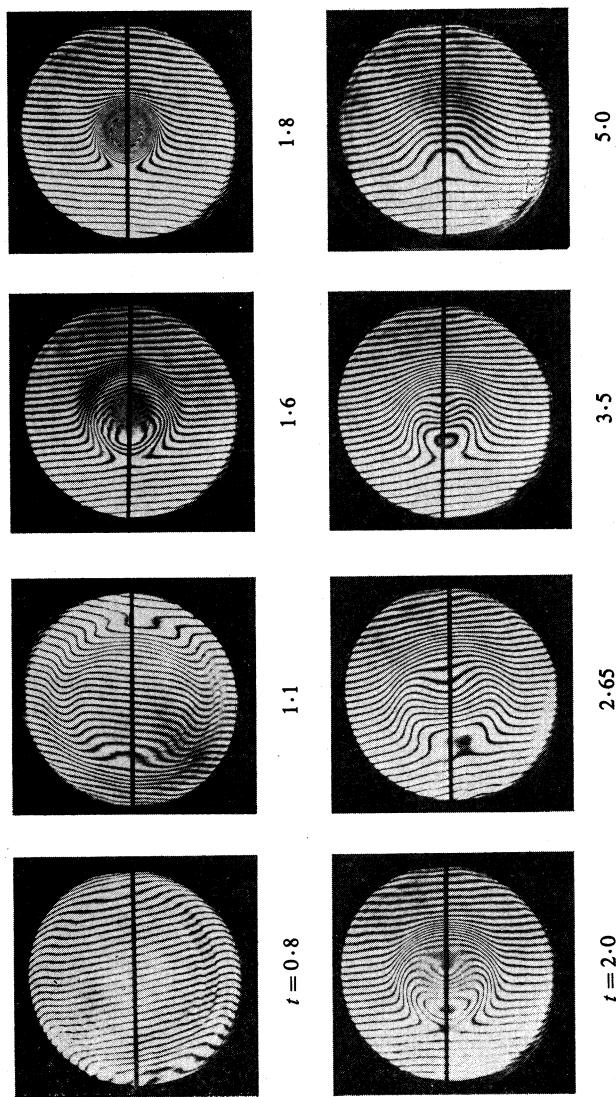


Fig. 11. Holographic interferograms recorded at different times (in μs) after commencement of the main discharge current for 35% preionization.

It is also important to note that each profile results from a density determination for only one discharge. Despite this limitation it appears that the $T_e + T_i$ profile is quite strongly dependent on the preionization level.

5. Summary and Discussion

(a) Formative Phase

After initiation of the main discharge current, the power input to the plasma rises in $\sim 1 \mu\text{s}$ to a peak value of $\sim 450 \text{ MW}$. The shape of this initial power input is insensitive to the degree of preionization.

The influence of the level of preionization on the characteristics of the initial implosion has been referred to in Section 4 where it was noted that at low levels of preionization there is rapid penetration of the magnetic field to the centre of the discharge. However, for 35% preionization this penetration is less rapid and there is a clearly defined imploding axial current sheet as indicated by the shapes of the B_θ profiles shown in Fig. 7. One observes that compression of the density (Fig. 12) and of the axial magnetic field (Fig. 6) occur just ahead of the imploding current sheet; there is a well-defined imploding shock for the higher levels of preionization.

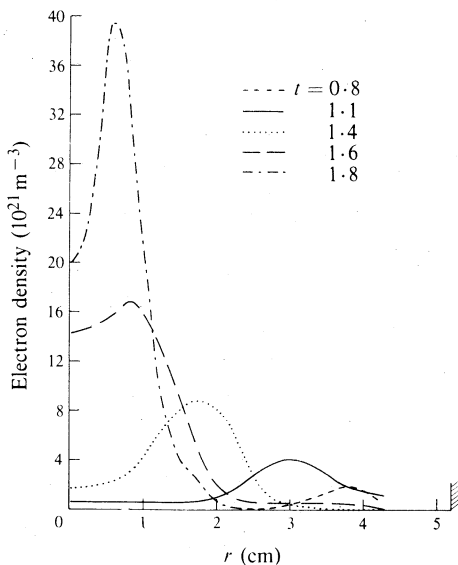


Fig. 12. Electron density profiles at different times t (in μs) during the implosion for the 35% preionization case. (The profile at $t = 1.6 \mu\text{s}$ is subject to some uncertainty near the axis because of the blurred nature of the fringes in this interferogram.)

Despite differences in the nature of the implosion, the time to reach peak compression (maximum B_z on-axis and minimum plasma radius) is essentially independent of the preionization level and lies in the range $\sim 1.7\text{--}1.8 \mu\text{s}$. At peak compression the electron density profiles are very hollow, and their general shape is relatively insensitive to the preionization level. The peak value of the density, however, decreases markedly at low preionization levels.

The 'bouncing' of the plasma following this initial compression is reflected in substantial and rapid variation in the on-axis axial magnetic field. The main features of this effect are summarized in Fig. 9 from which it is seen that the bouncing is more pronounced at higher preionization levels as noted in the streak photographs and power measurements (Figs 4 and 5).

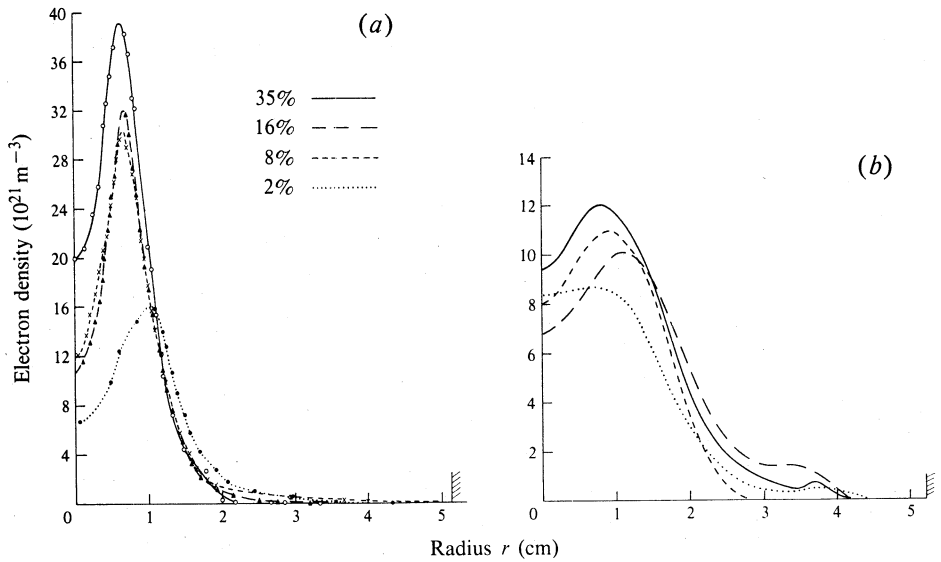


Fig. 13. Electron density profiles at (a) $t = 1.8 \mu\text{s}$ and (b) $t = 3.5 \mu\text{s}$ for the four levels of preionization.

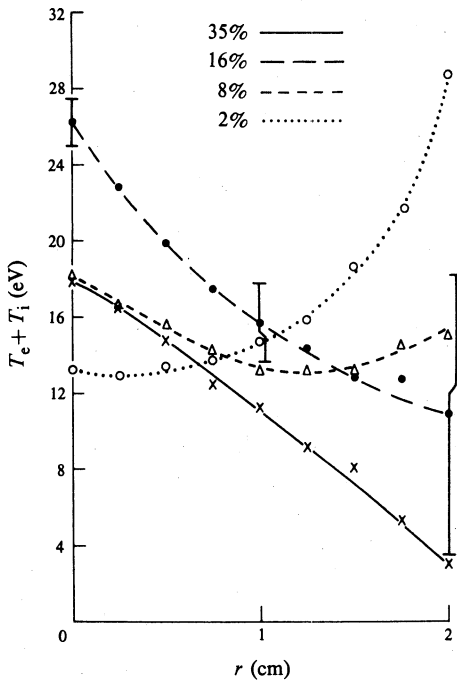


Fig. 14. Radial profiles of $T_e + T_i$ at $t = 3.5 \mu\text{s}$ for the four levels of preionization. Error bars shown are representative of the systematic uncertainty arising from the asymmetry in the B_θ profiles.

(b) Equilibrium Phase

The influence of the level of preionization is, generally speaking, less marked for the equilibrium phase than for the formative phase. Perhaps the least affected quantity is the on-axis axial magnetic field whose equilibrium value is, as shown in Fig. 9, essentially independent of the level of preionization.

Inspection of Fig. 13*b* reveals that the density profile is still hollow at $t = 3.5 \mu\text{s}$ (i.e. at 'equilibrium') for all levels of preionization. The differences between the profiles at this time are much less marked than at peak compression (Fig. 13*a*). While the density profiles are hollow for all levels of preionization, there are systematic differences between the pressure profiles: for 2% preionization, the profile is hollow and quite broad; the other three profiles are peaked on-axis and become progressively narrower as the level of preionization increases.

The broadening of the pressure profile with decreasing preionization is associated with a significant variation in the radial profile of $T_e + T_i$ with level of preionization (Fig. 14): the strongly shock-heated plasma (which results when the level of preionization is sufficiently high) develops a temperature profile which is strongly peaked on-axis.

The equilibrium phase is terminated by the onset of a macroscopic instability 6–10 μs after the start of the plasma current. The characteristics of the instability are not the object of the present study. It is worth noting however that there was little evidence to suggest that the onset of instability was markedly affected by the level of preionization (in contrast to the SPICA results of Bobeldijk *et al.* 1978 and the ZT-1 results of Baker *et al.* 1972).

In this regard it is of interest to calculate β_θ , defined by

$$\begin{aligned}\beta_\theta &= \frac{1}{\pi r_p^2} \int_0^{r_p} p(r) 2\pi r \, dr \bigg/ \frac{B_\theta^2(r_p)}{2\mu_0} \\ &= \frac{(4\pi)^2}{\mu_0 I_z^2} \int_0^{r_p} p(r) r \, dr,\end{aligned}$$

where r_p is the plasma radius when the plasma pressure $p(r)$ has fallen to zero and I_z is the total axial plasma current. The integral may be calculated using the pressure profiles determined from the magnetic field data to yield the following values of β_θ at 3.5 μs :

Preionization (%)	35	16	8	2
β_θ	0.49 ± 0.06	0.56 ± 0.09	0.59 ± 0.07	0.66 ± 0.05

It is concluded from the results reported here that the possibility exists of using varying levels of preionization to tailor radial profiles of density and pressure, and hence to influence the average value of β_θ .

Acknowledgments

The authors thank Dr F. C. Jahoda for his advice on the technical details of holographic interferometry. This work was supported by grants from the Australian Institute of Nuclear Science and Engineering and the Australian Research Grants Committee, and by the Australian Atomic Energy Commission.

References

- Ashby, D. E. T. F., and Jephcott, D. F. (1963). *Appl. Phys. Lett.* **3**, 13.
 Baker, D. A., *et al.* (1973). Proc. 6th European Conf. on Controlled Fusion and Plasma Physics, Moscow, Vol. 1, p. 293 (Joint Institute for Nuclear Research: Dubna).
 Bobeldijk, C., *et al.* (1978). Rijnhuizen Report No. 78-112.

- Burkhardt, L. C., *et al.* (1972). Proc. 2nd Topical Conf. on Pulsed High-Beta Plasmas, Garching Report No. IPP 1/127.
- Gowers, C. W., *et al.* (1972). Proc. 2nd Topical Conf. on Pulsed High-Beta Plasmas, Garching Report No. IPP 1/127, paper A4.
- Green, T. S., Newton, A. A., and Segre, S. E. (1966). *Nucl. Fusion* **6**, 223.
- Gribble, R. F., *et al.* (1974). Proc. 5th Int. Conf. on Plasma Physics and Controlled Nuclear Fusion Research, Tokyo, Vol. 3, p. 381 (I.A.E.A.: Vienna).
- Jahoda, F. C., and Sawyer, G. A. (1971). In 'Methods of Experimental Plasma Physics', Vol. 9 (Ed. R. H. Lovberg), Part B, p. 1 (Academic: New York).
- Jones, I. R., and Silawatshananai, C. (1980). *Plasma Phys.* **22**, 501.
- Koppendorfer, W. (1963). Proc. 6th Int. Conf. on Phenomena in Ionized Gases, Paris, Vol. 2, p. 545.
- Krause, H., Wilhelm, R., and Zwicker, H. (1973). Proc. 6th European Conf. on Controlled Fusion and Plasma Physics, Moscow, Vol. 1, p. 273 (Joint Institute for Nuclear Research: Dubna).
- Newton, A. A., Gowers, C. W., Nalesso, G. F., Robinson, D. C., and Bodin, H. A. B. (1972). Proc. 5th European Conf. on Controlled Fusion and Plasma Physics, Grenoble, Vol. 1, p. 44 (Euratom—C.E.A.: Grenoble).
- Weber, P. G., Brennan, M. H., Jones, I. R., Murray, E. L., and Silawatshananai, C. (1976). *Bull. Am. Phys. Soc.* **21**, 1056.

Manuscript received 13 March 1980, accepted 1 July 1980

